JOURNAL OF GEOPHYSICAL RESEARCH, VOL. 113, A00A15, doi:10.1029/2008JA013224, 2008

Solar Mass Ejection Imager 3-D reconstruction of the 27–28 May 2003 coronal mass ejection sequence

B. V. Jackson,[1] M. M. Bisi,[1] P. P. Hick,[1] A. Buffington,[1] J. M. Clover,[1] and W. Sun[2]

Received 31 March 2008; revised 17 July 2008; accepted 16 September 2008; published 18 December 2008.

[1] The Solar Mass Ejection Imager (SMEI) has recorded the inner-heliospheric response in white-light Thomson scattering for many hundreds of interplanetary coronal mass ejections (ICMEs). Some of these have been observed by the Solar and Heliospheric Observatory (SOHO) Large-Angle Spectroscopic Coronagraph (LASCO) instruments and also in situ by near-Earth spacecraft. This article presents a low-resolution three-dimensional (3-D) reconstruction of the 27–28 May 2003 halo CME event sequence observed by LASCO and later using SMEI observations; this sequence was also observed by all in situ monitors near Earth. The reconstruction derives its perspective views from outward flowing solar wind. Analysis results reveal the shape, extent, and mass of this ICME sequence as it reaches the vicinity of Earth. The extended shape has considerable detail that is compared with LASCO images and masses for this event. The 3-D reconstructed density, derived from the remote-sensed Thomson scattered brightness, is also compared with the Advanced Composition Explorer (ACE) and Wind spacecraft in situ plasma measurements. These agree well in peak and integrated total value for this ICME event sequence when an appropriately enhanced (~20%) electron number density is assumed to account for elements heavier than hydrogen in the ionized plasma.

Citation: Jackson, B. V., M. M. Bisi, P. P. Hick, A. Buffington, J. M. Clover, and W. Sun (2008), Solar Mass Ejection Imager 3-D reconstruction of the 27–28 May 2003 coronal mass ejection sequence, *J. Geophys. Res.*, *113*, A00A15, doi:10.1029/2008JA013224.

1. Introduction

[2] The 27–28 May 2003 halo coronal mass ejection (CME) sequence was one of the first tracked by the Solar Mass Ejection Imager (SMEI) from near the Sun as an interplanetary coronal mass ejection (ICME) out to beyond the distance of Earth [*Tappin et al.*, 2004; *Jackson et al.*, 2004] and also viewed by the Solar and Heliospheric Observatory (SOHO) Large-Angle Spectroscopic Coronagraph (LASCO) [*Brueckner et al.*, 1995]. In the SMEI analyses an ICME was observed as outward moving brightness surrounding the Sun in SMEI sky maps differenced either from a previous map, or from a long-term mean average of maps. The ICME leading edge was observed advancing outward over a period of about day starting early on 29 May 2003. In these images some auroral brightness overwhelms the ICME signals during the time in its orbit that SMEI passes through the Earth's auroral ovals, from late 29 May until mid-day on 30 May.

[3] SMEI [*Eyles et al.*, 2003; *Jackson et al.*, 2004] was launched 6 January 2003 on the Air Force Space Test Program satellite Coriolis. The instrument consists of three baffled cameras whose $3^\circ \times 60^\circ$ fields of view are aligned in the long dimension to achieve a combined $\sim 160^\circ$ wide field of view that scans most of the sky every 102-min orbit (Figure 1). The cameras view the heliosphere in Thomson-scattered light with $\sim 0.5^\circ$ angular resolution. Approximately 4500 four-second-exposure CCD-camera data frames per orbit as in Figure 2a are combined into a map of the sky as shown in Figure 2b. Using a combination of three-dimensional (3-D) modeling and image-analysis techniques, SMEI observations quantify the 3-D extents of transient structures and their interactions with each other and with slow-moving ambient solar wind. These techniques have mapped the 3-D extents of the 28 October 2003 halo ICME in low resolution and determined its mass [*Jackson et al.*, 2006]. Other studies [*Yu et al.*, 2005; *Jackson et al.*, 2007a, 2007b] have mapped the 3-D extent of the high-velocity structure surrounding the 28 October 2003 ICME and determined the energy present in its outward flowing material.

[4] This article uses the term "CME" in reference to a sequence of events in the low corona as viewed in the LASCO observations, but in keeping with the now common terminology for these, describes these events in the interplanetary medium as "ICMEs"; the switch occurring when this material is viewed by SMEI and measured in situ near Earth.

[5] Section 2 describes the analysis developed by our group at the University of California at San Diego (UCSD) that removes auroral and high-energy-particle residues from the SMEI brightness data, generates photometric sky maps, and prepares data from these into time series suitable for the 3-D density reconstruction. Section 2 also briefly describes

[1] Center for Astrophysics and Space Sciences, University of California, San Diego, La Jolla, California, USA.
[2] Geophysical Institute, University of Alaska, Fairbanks, Alaska, USA.

0148-0227/08/2008JA013224$09.00

Figure 1. SMEI is depicted on the Coriolis spacecraft in its terminator polar orbit at 840 km with an orbital inclination of 98°. SMEI looks away from the Earth at 30° above the local horizontal to avoid sunlight reflected from the Earth and from the Windsat radiometer antenna situated at the top of the Coriolis spacecraft. The fields of view of the three cameras (each shown as shaded wedges extending from the satellite in this artist's impression) together cover nearly 180° of sky and, as the instrument orbits Earth, sweep out nearly the whole sky around it.

the 3-D reconstruction using these brightness time series. Section 3 presents the results of these analyses for the 27–28 May 2003 event sequence, the 3-D locations of various portions of the ICME, its volume, and the mass and energy associated with its outflow. Section 4 compares these results with SOHO/LASCO data and with in situ observations. The ICME is manifest as a large density enhancement at ~1 AU for spacecraft situated near the Earth. We conclude in section 5.

2. SMEI Analysis Techniques

2.1. UCSD SMEI Data Processing

[6] Telemetry data from SMEI are relayed to several Air Force Research Laboratory (AFRL) sites and then via FTP transfer to UCSD where individual CCD frames are decompressed and combined with pointing information from the Coriolis onboard star tracker. At UCSD we maintain a database in near-real time on a local server and as quickly as possible a UCSD analysis sequence processes individual SMEI data frames and generates a heliospheric sky map and additional higher-level data products for every 102-min SMEI orbit (see http://smei.ucsd.edu). Star-tracker information places each data frame generally within 0.05° of its sidereal location, and this provides sufficient accuracy for the removal of stellar signals in the final sky maps [see *Hick et al.*, 2007]. (There is an occasional loss of accurate star-tracker pointing control on some (~10%) of the SMEI orbits for short periods of time that can amount to star-tracker pointing errors of up to several degrees. This loss of star-tracker signal lock appears generally in the SMEI sky maps as incorrectly subtracted stellar signals usually in the southern portion of the sky.) These maps retain the SMEI data frame resolution, and are provided with either stars present or stars removed, and are optimized for photometric accuracy. These high-resolution sky maps allow further data processing for star-like bright points and allow for better star removal algorithms at a later date should these become available. In contrast, the sky maps currently retained by the AFRL and the National Solar Observatory (NSO) (see http://smei.nso.edu/index.html) have a resolution of about 0.5 degrees, more nearly commensurate with the size of the SMEI point spread function. In addition to the data sequence described by *Hick et al.* [2005, 2007], we further clean each sky map of residual high-energy-particle hits, some of the stray light near the moon and the bright planets, and some of the bright auroral light [see *Jackson et al.*, 2006] that is an unexpected and major contributor [see *Mizuno et al.*, 2005] to the SMEI measurements.

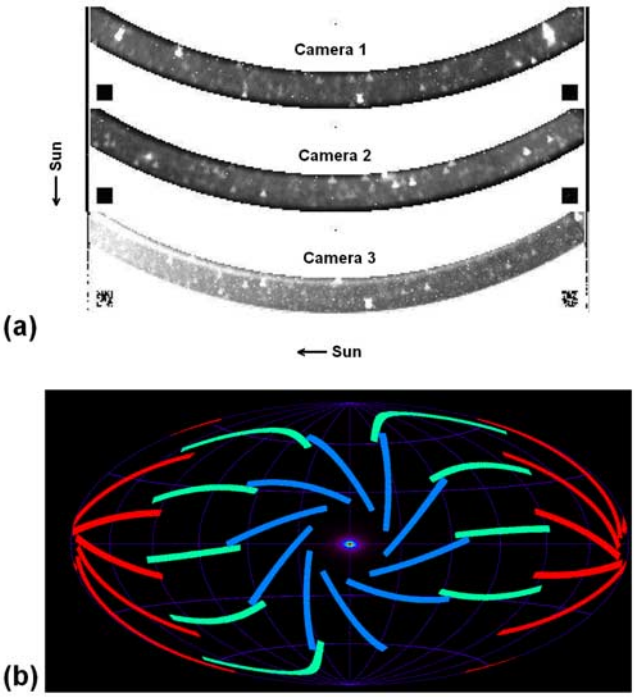

Figure 2. (a) These are 3° × 60° image frames from each of the three SMEI cameras: Camera 1 (top) views farthest from the Sun, and camera 3 (bottom) views closest, with the Sun toward the left in each frame. (b) Full-sky Hammer-Aitoff projection showing the placement of a sample of SMEI camera image frames with the Sun centered in the projection (in October). About 4500 frames per orbit fill in the sky in a clockwise direction every 102 min. Camera 1 is shown in red, Camera 2 is in green, and Camera 3 is in blue.

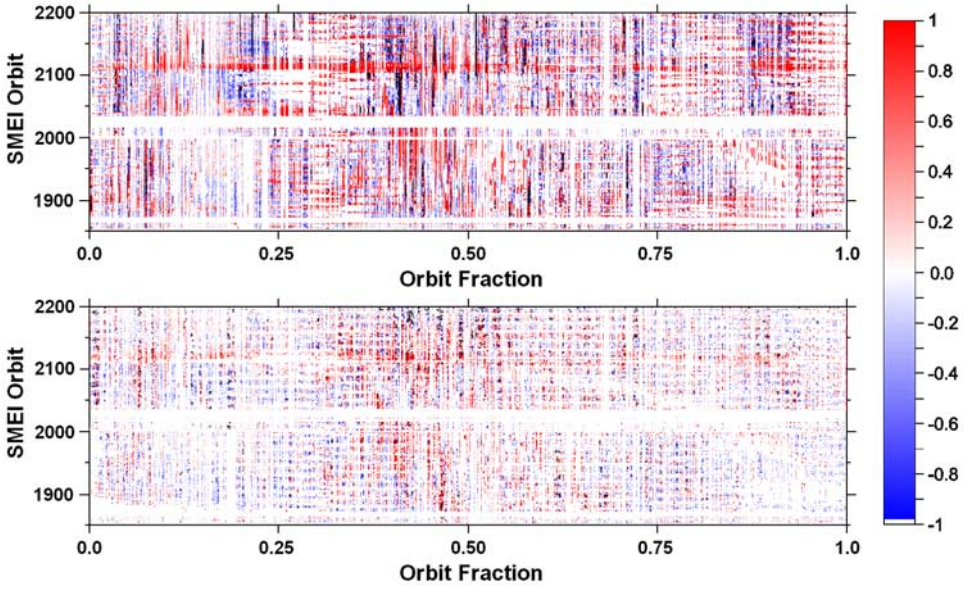

Figure 3. SMEI time series Analog-to-Digital Unit (ADU) brightness displayed as orbit versus orbit fraction (approximately) for the May ICME time interval. (top) Time series brightness edited to eliminate only the most significant excursions from a mean value. Low-level auroral light and some high-energy-particle hits have not been removed. These include twice-daily contamination from the South Atlantic Anomaly which appear as horizontal red bars near orbit fraction 0.3 and from 0.8 to 1.0. (bottom) Time series with most noise removed as described in the text. The remaining valid excursions from zero (from ~110,000 lines of sight during the interval) are the Thomson-scattered signal differenced from a long-term average base brightness. The 27–28 May 2003 CME is recorded as an ICME on orbits 2110–2150.

[7] Since light from the zodiacal-cloud brightness [*Buffington et al.*, 2006b] plus the sidereal sky (stars, the Milky Way, bright nebulae, and galaxies) is a factor of 100 greater than the variable heliospheric Thomson-scattered signal [see *Jackson et al.*, 2004], contributions from these must be subtracted carefully from the orbital sky maps. The simplest way to remove these presumed slowly changing components is by subtracting Sun-centered sky maps from orbits adjacent or not too distant in time (''running differences''); in this case any constant heliospheric signal that is present in both orbits cancels in the difference map, so in effect only short-term changes in the heliospheric signal are retained. *Tappin et al.* [2004] used orbit-to-orbit differences from the previous sky map to display observations of the heliospheric response to the 27–28 May 2003 halo-CME event sequence, which is analyzed in more detail here. More than 300 ICMEs have been observed in the SMEI data to date by this method; most of these are likely associated with CMEs observed also in SOHO/LASCO data [*Webb et al.*, 2006].

[8] At UCSD to retain more slowly changing portions of the heliospheric signal, we remove background light in steps that separate the component signals into sidereal and heliocentric components. We first remove a two-dimensional modeled zodiacal-light map [*Buffington et al.*, 2006b] in heliographic coordinates. We then remove a sidereal brightness map from the residue in sidereal coordinates. We further remove a median filtered minimum map currently from 600 consecutive SMEI orbits in polar heliocentric coordinates. A selection of lines of sight from the sidereal sky map is chosen to be both separated from one another by approximately 3° and located to avoid bright stars in order that difficulties in their removal not influence our photometric result. These ~4000 sky locations are averaged to one-square-degree sections of the sky, and culled down to ~1000 to emphasize the population of lines of sight in the solar direction. This remaining collection of line-of-sight time series is then ready to proceed to further analysis.

[9] First, each line-of-sight time series is cleaned of unwanted residues (left-over high-energy-particle contamination, auroral light or veiling glare from the moon) by eliminating signals too large to be Thomson-scattering brightness changes. Next, an average Gaussian mean brightness with an e^{-1} weighting 200 orbits (~14 days) from the midpoint time is subtracted and the residual is presented as a two-dimensional orbit-versus-time-in-orbit map. This map is normalized so that each point has approximately the same weight by normalizing brightness to solar elongation (ε) by multiplying each point by $\varepsilon^{2.5}/90^{2.5}$. This is an empirical approximation to a correction of the brightness falloff with elongation shown by *Jackson et al.* [2004] (Figure 3). The map is then filtered using a several-step iterative process that eliminates the largest discrepant excursions from the mean value in time and at adjacent orbital locations and then recalculates the mean and again eliminates outliers using a more stringent criterion as illustrated in Figure 3. At each step a new long-term average Gaussian mean is calculated as well as a rapidly time-varying filter that follows the rapid excursions from the mean. Excursions greater than approximately two standard deviations from this rapidly varying filtered data set are removed from the time series. The filter parameters on each step have been set such that typically 5% of the remaining time series data points are eliminated

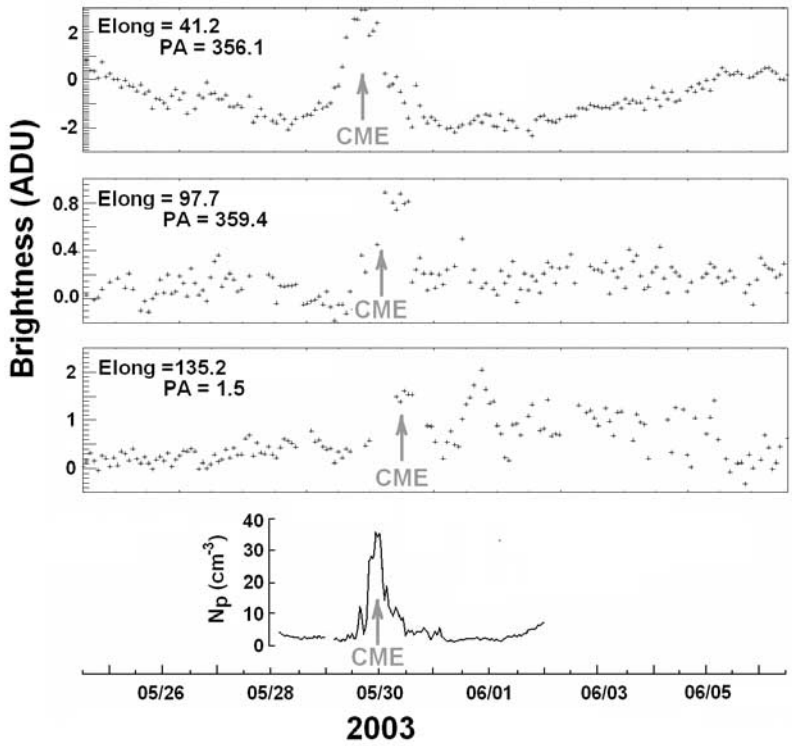

Figure 4. Measurements obtained during the 27–28 May 2003 halo ICME. The three top plots show examples of SMEI brightness time series in ADU (at 102-min intervals) from individual square degrees of sky at different angular distances from the Sun, after removing a long-term base as in Figure 3b. The bottom plot shows 1-h average proton density from ACE level 0 data.

on each iteration with fewer and fewer data points remaining in the time series.

[10] At the end of the above filtering sequence discrepant high and low values in the time series at the ~1000 sidereal locations (see above) are removed such that only excursions of a few CCD Analog-to-Digital Units (ADUs) from the mean normalized to the 90° elongation value remain in the record. If too few data points remain at a time series location in the original data set (usually fewer than 25%), that sidereal location in the sky is no longer used in the analysis. This current UCSD-designed analysis provides a final stable base and variable time series over time scales of many weeks which are adequately free of most unwanted noise for the 3-D reconstructions presented here. About half of the time series data points eliminated in the final time series analysis are simply too discrepant from the mean to be Thomson-scattered light, and are primarily caused by aurora and high-energy-particle contamination not removed by editing techniques available during the sky-map generation process. The additional filtering typically removes about half of the remaining line of sight data points. These are generally near the edges of the regions of high data brightness signals from the mean previously identified (see Figure 3, top).

[11] Figure 4 presents sample time series from the sky measurements used for the analysis of the May–June 2003 time period that includes the 27–28 May ICME sequence. Brightness for these data are given in SMEI ADUs, and a typical one-sigma noise level in a square degree of sky for an individual measurement at 90° for these measurement in regions free of aurora and high-energy-particle hits is about 0.14 ADU, or close to the photon noise limit [*Buffington et al.*, 2006a]. A more natural unit for surface brightness in the present work is "S10", the equivalent brightness of a tenth magnitude solar-type star spread over one square degree of sky. Calibration of SMEI data using 17 bright stars also well measured in LASCO [*Buffington et al.*, 2007] gives 1 S10 = 0.46 ± 0.02 ADU for SMEI Camera 2. Relative brightness in the two other SMEI cameras is also determined to approximately this same precision by the same method; these are normalized to Camera 2 by multiplying Camera 1 and Camera 3 observed brightness by factors of 0.97 and 0.92, respectively. A slight absolute decrease in CCD stellar response of 1% per year for all cameras is also corrected in this analysis as determined by consistently removing the galactic center brightness residual over five years of SMEI data. The ~1000-member time series in turn produces approximately 110,000 valid lines of sight over a time interval from 11 May to 7 June 2003; this interval includes the ICME arrival at Earth on 29 May 2003. This number of lines of sight is sufficiently redundant to support 3-D reconstruction at the resolution described below.

2.2. Three-Dimensional Reconstruction Analysis

[12] The computational aspects of the 3-D reconstruction program are discussed more fully by *Jackson et al.* [1998], *Kojima et al.* [1998], *Hick and Jackson* [2004], *Jackson et al.* [2006], and references therein. More recently [*Jackson et al.*, 2001, 2002; *Jackson and Hick*, 2004], the assumption that the structure corotates has been relaxed. Briefly, how-

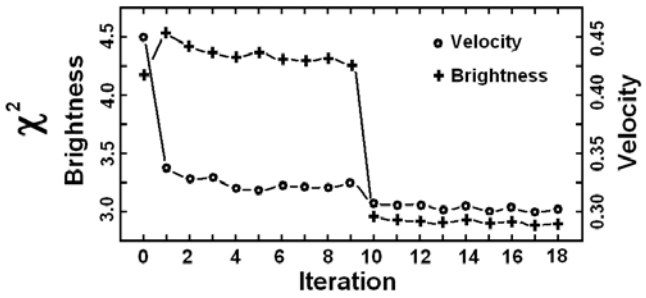

Figure 5. Rate of convergence as measured by the χ^2 difference between modeled and observed line-of-sight brightness and velocity for each iteration throughout the 4-week measurement interval in which the 27 May 2003 event sequence is centered. The sudden drop in χ^2 difference in brightness seen after iteration 9 results from discarding the lines of sight that do not fit within a three-sigma limit as described in the text.

ever, line-of-sight segments and their 3-D weights are projected back in space and time to a solar wind inner boundary (source surface) that is set at 15 Rs in these analyses. Here these values are iteratively inverted on the two-dimensional inner boundary at the different time steps to provide solar wind model outflow parameters. In current analyses the inversion process updates boundary conditions for the kinematic 3-D solar wind model to better fit observations using a least squares fitting procedure. This procedure minimizes the differences between modeled and observed brightness, and also the differences between modeled and observed IPS velocity, this latter data from the Solar Terrestrial Environment Laboratory (STELab), Nagoya University, Japan. As explained elsewhere [i.e., *Jackson and Hick*, 2002, 2004], it is not possible to distinguish the ambient solar wind Thomson scattering signal from the small percentage of the zodiacal light brightness signal this constant ambient produces. Because of this, the mean value for this ambient is modeled using the average in situ density measured from the mean solar wind value at 1 AU throughout the period of the observation.

[13] In the least squares fitting process, ratios of model-to-observed values and a modeled-to-observed χ^2 are monitored at each iteration (Figure 5) to indicate a rate of convergence for this interval. Here, velocity and density corrections to the model are made separately. First, changes are made to previous velocity boundary conditions on the inner boundary surface. Second, the 3-D solar wind model is updated and new projected locations of each line-of-sight point on the inner boundary surface are determined. Third, changes are made to previous density boundary conditions on the inner boundary surface. Finally, the 3-D model is again updated with all the newest boundary values.

[14] The inner boundary Carrington maps of velocity and density are smoothed for each iteration using a 2-D Gaussian spatial filter that incorporates equal-solar-surface areas, and a Gaussian temporal filter. These filters for the 27–28 May 2003 analysis, and the digital coordinate resolutions are identical to those used for the 28 October, 2003 ICME [see *Jackson et al.*, 2006] which are spatially in heliographic latitude and longitude 6.7° × 6.7° with a half-day temporal cadence. This approximately matches the Gaussian filter resolution [*see Jackson and Hick*, 2004]. The locations in the model where the model values cannot be changed as above are left blank in the final result. For the analysis presented here, the blank areas include sections of heliospheric volume on the opposite side of the Sun from Earth that cannot be observed and reconstructed by SMEI at the digital resolutions used. No blank areas appear in the earthward hemisphere using this criterion.

[15] The reconstruction program generally converges to an unchanging model within a few iterations, but is set to operate for 9 iterations to guarantee convergence [see *Jackson et al.*, 1998]. For a typical rotation and the digital resolutions stated earlier, a set of density and velocity iterations generally takes about fifteen minutes on a 3.0 GHz Intel® Pentium IV™ computer. Those IPS-velocity observations and SMEI-brightness lines of sight throughout the period that do not fit within a three-sigma limit of the mean ratio change ascribed at that location by the model (typically, and in this instance, 1.3% of the brightness line-of-sight data points) are removed from the data set. This allows a further safeguard for the removal of lines of sight outliers that do not fit the model values, and in this case we find that the overall χ^2 fit for brightness is significantly reduced when this criterion is evoked (see Figure 5). The program then operates for 9 more iterations (18 in total). The solutions are insensitive to the initial model values, and

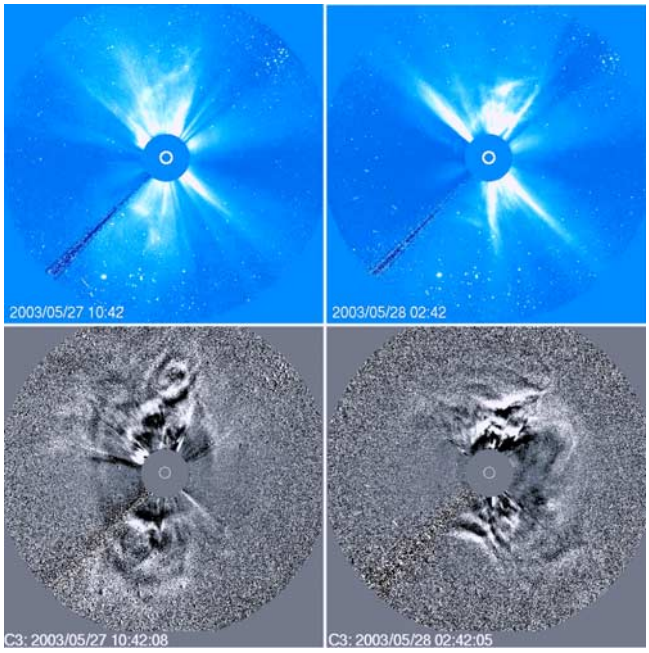

Figure 6. SOHO/LASCO C3 coronagraph (top) direct and (bottom) difference images of the dominant halo CMEs that are reported on 27 May and 28 May 2003. The halo CME of 27 May was first observed in the C2 coronagraph at 0650 UT traveling at a speed of 500 km s^{-1}. The second halo CME group was observed on 27 May at 2206 UT and 2350 UT and on 28 May at 0050 UT traveling at sky-plane speeds of 1122, 964, and 1366 km s^{-1}, respectively. On 28 May several earlier CMEs are observed superimposed on one another in the images.

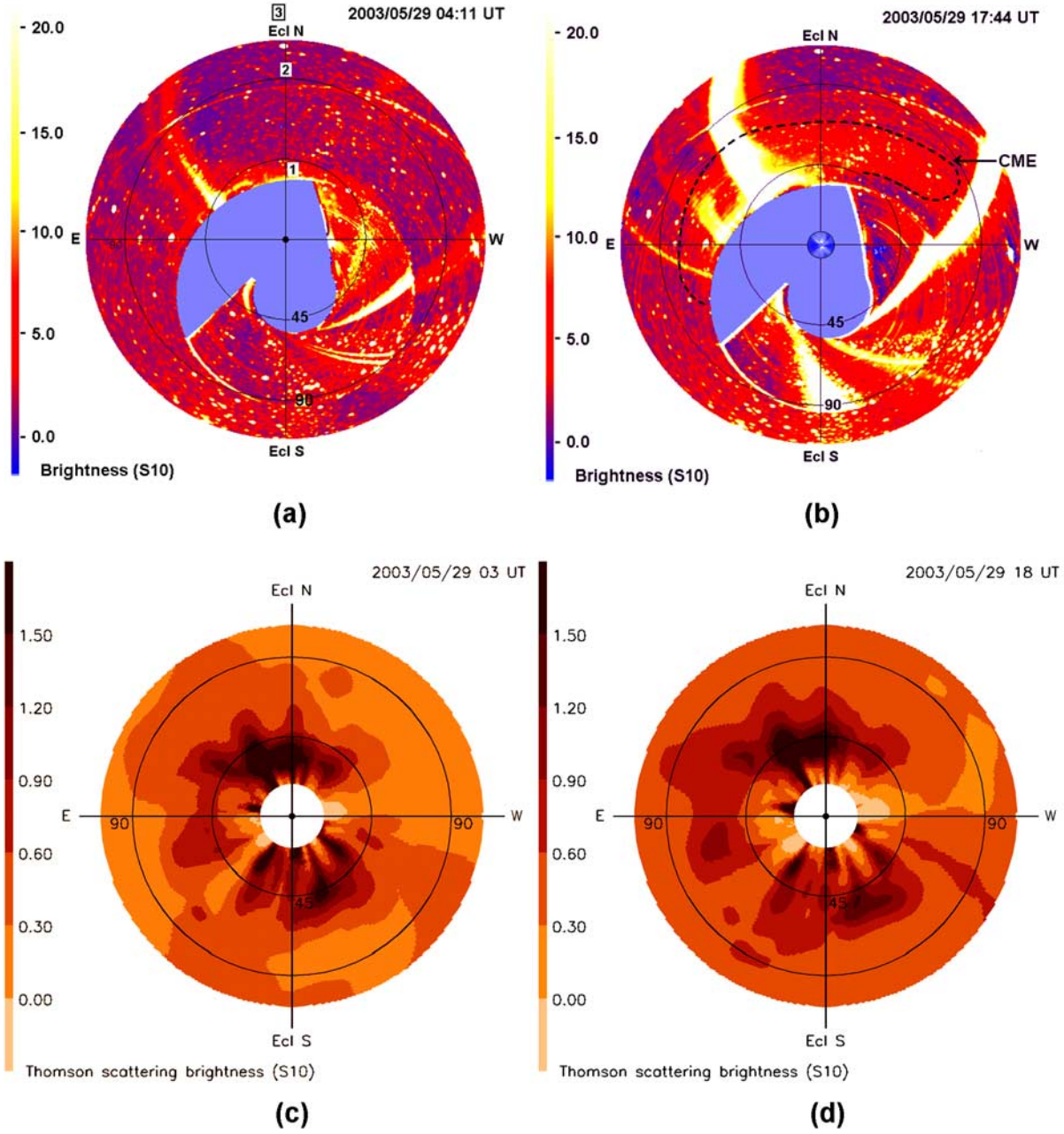

Figure 7. Brightness increase of the ICMEs as they move outward from the Sun. (a and b) Direct SMEI sky map images on 29 May 2003. Shown are two orbits of data differenced from an 8-orbit average for SMEI cameras 1, 2, and 3. The white bands in the sky maps that extend roughly outward from the center are primarily locations where bright auroral light obscures the photometric signal. Areas without SMEI data in the center of the images are shown in deep blue. The data were smoothed using a 1° Gaussian filter. The specks in each image are stellar signals, mostly bright stars with apparent changed brightness over the observation interval. Brightness is in S10 units as converted from ADU (see text). A SOHO/LASCO C3 coronagraph image is inserted in the top right map for a comparison of the observing scale. Numbered locations 1–3 in the top left map indicate the regions shown as time series in Figure 4. (c and d) The approximate same images showing far better defined features and the halo enhancement surrounding Earth that are obtained from time series modeling that can now be presented at an order of magnitude finer brightness scale.

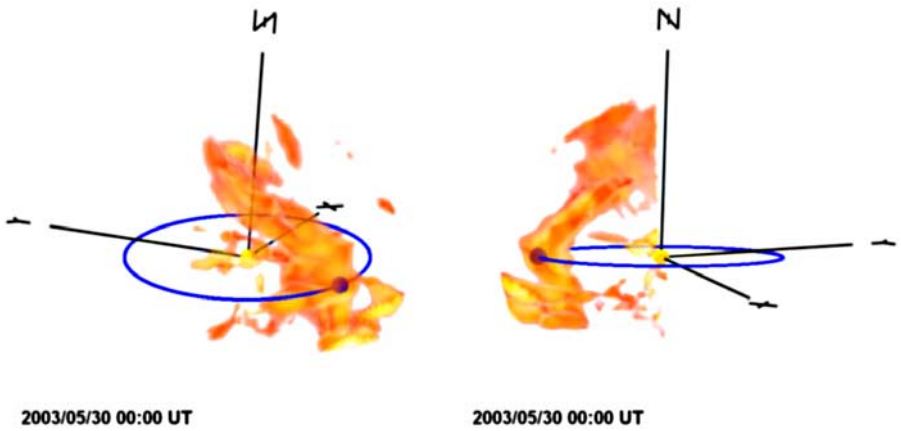

Figure 8. Remote observer views of the 27–28 May 2003 halo-CME/ICME sequence displaying 3-D density reconstruction from two different perspectives as seen as from infinity at 0000 UT on 30 May 2003 just as the ICME engulfs the Earth. Density is plotted upward from 12.0 protons cm^{-3}. Earth orbit is shown as a blue ellipse with the Earth a sphere engulfed in the event. The axes are heliographic coordinates with +X direction pointing toward the vernal equinox and +Z toward solar heliographic north. An r^{-2} density falloff has been removed from the analysis to better show structures at increasing distance from the Sun. (left) Density viewed ~20° above the ecliptic and ~45° east of the Sun-Earth line and (right) ~5° above the ecliptic and 90° west.

after a few iterations any residual signature of the initial values has disappeared. Other tests [see *Jackson et al.*, 1998] show that the 3-D reconstruction of a set of artificial observations using a known 3-D input reproduces the input.

3. Three-Dimensional Analysis Results

3.1. Coronagraph Images and Direct Sky Maps

[16] SOHO/LASCO C3 coronagraph images of the 27 and 28 May CMEs are shown in Figure 6. The coronagraph images during this interval show several halo CMEs with considerable structure and mass combined with background coronal features. The first of these events moves out slowly such that the latter, having started about 18 h later but having over twice the outward expansion rate, has caught up with the first on their way to Earth. Figures 7a and 7b show direct SMEI "fisheye" sky maps obtained from single orbits of data as the May 2003 ICME arrives at Earth midday on 29 May. The beginning time of the data producing each sky map is indicated to the upper right of the map, and for this display proceeds clockwise around map center from the southernmost point of the map as described in Figure 2b. The brightness scale to the left of the map is in S10 (see section 2.1, final paragraph). Portions of the sky maps are blanked out where too many high-energy-particle hits and/or too much auroral light produce an apparent response far above the normal background. The location of the brightest portion of the ICME change to the north from the Figure 7a sky map is outlined by a dashed line from the previous image shown in Figure 7b.

3.2. Three-Dimensional Reconstructed Sky Maps

[17] Figures 7c and 7d present a sequence of modeled fisheye sky maps and show the progression of the 27–28 May 2003 ICMEs outward in 2-D sky maps. The sky maps are derived from the 3-D reconstructed density volumes that have been fit to the observed data by integrating through the volumes and summing the total line-of-sight brightness [*Billings*, 1966] as is required to match modeled to observed brightness in the direct sky maps. The times given in Figures 7c and 7d, on subsequent SMEI reconstructions and in tables, are instantaneous times interpolated to the appropriate value from the reconstruction analyses. The brightness includes the r^{-2} heliospheric density falloff, and thus provides brightness as observed in direct images. The sky maps from the tomographic modeling have a base of 3.3 e^{-} cm^{-3} at 1 AU removed from them that is also modeled with an r^{-2} heliospheric density falloff, and show excursions from a mean of zero, in order to match the time series of Figure 4 or the direct images of Figures 7a and 7b, where all but the changing brightness has been removed. Since the fit to a heliospheric solar wind model uses time series from multiple sky maps, and reduces signals that do not participate in the outward progression of the solar wind, gaps or bad spots in the data are filled in to provide continuous inner-heliospheric coverage. For most of the time period covered by the reconstructed sky maps, the area blanked out near the center of the direct sky maps of Figures 7a and 7b is located in approximately the same place. This region is back-filled somewhat, and more at some position angles than others to a circle set at 18° from the Sun. Since few non-heliospheric artifacts such as zodiacal light and aurora remain in these maps constructed from volumes from the edited time series, the image contrast of the map can be enhanced above that of direct sky maps, thus highlighting more detail. This analysis shows the bright heliospheric ICME response that engulfs the Earth. In sky maps the progression of some dense features move slowly outward distant from the Sun and Earth with some portions close to Earth progressing much more rapidly. Further, Figures 7c and 7d show the CME observed to the north in the LASCO C3 CME observations of Figure 6 (top left and bottom left) that has moved outward to about 45° elongation. Finally, they also show the dense portion of a CME listed as a partial

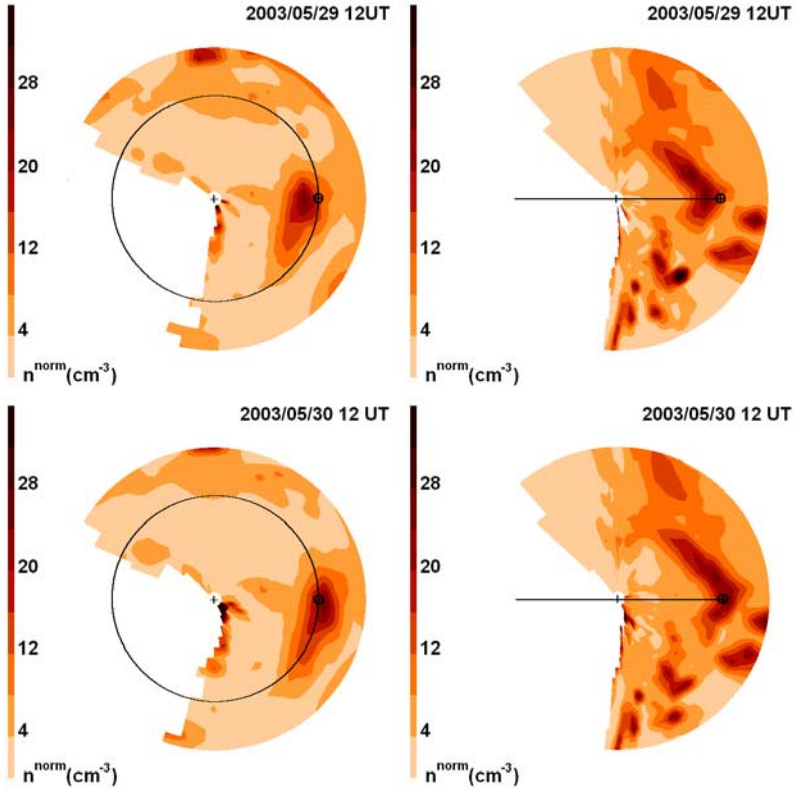

Figure 9. (left) Ecliptic and (right) meridian cuts of the 27–28 May 2003 ICME sequence before and after the ICME's dense structure passes Earth. Earth's orbit is shown as a circle or line with the Earth "⊕" indicated on each plot. As in Figure 8, an r^{-2} density falloff scaling normalizes structures at different radii. Density contours to the left of each image are scaled to 1 AU. Regions within the model that cannot be adequately determined by the 3-D reconstruction techniques described in section 2.2 are left blank in these cuts and are located primarily in the region opposite the Sun from Earth.

halo event to the solar southwest first observed late on 27 May 2003 that has moved outward to between 50° and 60° elongation.

3.3. Three-Dimensional Reconstructed Remote View Masses, Volumes, and Energies

[18] The 3-D density distribution from which these sky maps were derived permits the results to be viewed from any vantage point, not just from the Earth. Since several heliospheric structures often overlap along a line of sight, determination of their 3-D extent has the advantage of more completely allowing measurement of the direction of travel and the masses of structures over time. Figure 8 shows a 3-D reconstruction of the 27–28 May 2003 CME sequence just as the ICME structure engulfs Earth on 30 May 2003. The shell-like shape and the eastward extent of the ICME sequence are evident in these reconstructions but less evident in the direct images simply because the structure that engulfs Earth is only a portion of the whole. Figure 9 shows this same structure at 1200 UT on 29 May and at 1200 UT on 30 May 2003 in both ecliptic and meridional cuts just before and after the structure passes Earth. Views of heliospheric brightness from SMEI are at best viewed starting at 20° elongation, and no SMEI lines of sight directly explore the heliospheric hemisphere beyond the Sun as viewed from Earth closer than this angular distance. Thus, the portion of the heliospheric volume beyond the Sun away from Earth has not been completely reconstructed as is shown in these planar cuts. The 3-D resolution is presently limited by the numbers of lines of sight used in the analysis. There are several reasons that not all lines of sight are used at this time, and chief among these is a computational limitation; current 3-D reconstruction algorithms including the removal of auroral light (section 2.1), can easily handle only a total of ~300,000 lines of sight. The use of more lines of sight will ultimately increase the resolution of the reconstructed sky maps but is not expected to significantly affect the large-scale shape of the event, only enhance its detail. These reconstructions show that the mass of the ICME as it engulfed the Earth on 30 May at 0000 UT was structured similar to the views of the CME sequences in LASCO coronagraph images shown in Figure 6, with more massive portions of the ICME traveling to the north and south of the Sun. The main portion of the CME sequence that reaches Earth on 30 May 2003 is somewhat shell-like in appearance. Figure 10 shows the 3-D ICME mass determination (as described more fully for the 28 October 2003 ICME by *Jackson et al.* [2006] and *Yu et al.* [2005]) of the dense structure of the CMEs as they engulfed Earth. In these analyses a 3-D contour level is set to isolate the mass of the main structure from other heliospheric features, and the heliospheric structure is then

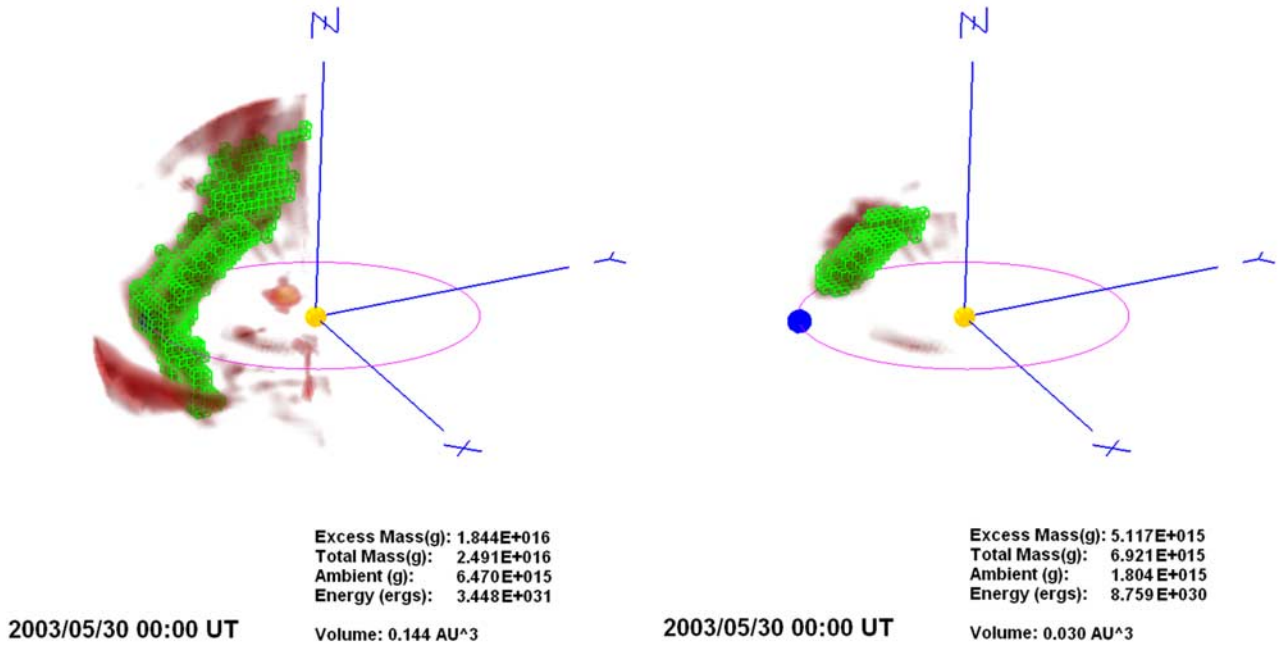

Figure 10. Three-dimensional mass determination for the 27–28 May 2003 halo CME sequence as the associated ICMEs reach Earth vicinity at 0000 UT 30 May 2003. Electron density is contoured upward from 15 cm^{-3}. (left) The total event is highlighted and filled with cubes, has a volume of 0.144 AU^3 above this contour interval, and has a total mass of 2.49×10^{16} g (see Table 2). (right) A small portion of the event as described in the text and shown in Table 2 has a volume of 0.030 AU^3 and total mass of 6.9×10^{15} g.

approximated by cubes throughout the volume within the contour. The sum of the mass within these cubes determines the total mass of the structure, and the summed volume of the cubes gives its total volume. To relate mass to numbers of electrons we assume (e.g., as did *Hildner et al.* [1975]) that one electron is associated with 2.0×10^{-24} g of material; this incorporates the usual 10% abundance of fully ionized helium by number relative to protons, and a negligible contribution from heavier elements [see *Cox*, 2000, section 3.2]. By assuming an ambient solar wind (5 e^- cm^{-3} at 1 AU with an r^{-2} falloff), we obtain a value of excess mass above ambient within this contour as the difference of the total mass and ambient. Table 1 presents the inferred volume of the enclosed structure, and its excess and total masses. The final column in Table 1 is the energy associated with the outward flow of this material using the 3-D reconstructed IPS velocity.

[19] These results presented in Table 1 are measured upward from two lower contour-level thresholds (12.0 e^- cm^{-3} and 15.0 e^- cm^{-3}) in order to demonstrate the sensitivity of the inferred ICME measurements at 1 AU to the amount of solar wind material assumed to be included in the events. This lower boundary is somewhat arbitrary. There are no extremely dense regions of the solar wind present in the reconstructions, and the lower of the two levels (12 e^- cm^{-3}) is the least practical threshold here for separating this ICME structure from the rest of the solar wind. The choice of the ambient value of 5 e^- cm^{-3} relates in direct proportionality to the amount of ambient mass present attributed to the ICME material, and decreases the excess mass attributed to the ICME material by the proportion included in the ambient. Since the bulk of the ICME mass is present from material far above the ambient and the excess generally comprises approximately three-quarters of the total ICME mass, there is not a large change of ICME excess mass caused by an error in the calculation of this ambient value.

Table 1. Three-Dimensional ICME Volumes, Masses, and Energy Derived for the 27–28 May 2003 CME Sequence

Lower Contour (e^- cm^{-3})	Volume (AU^3)	Excess Mass ($\times 10^{16}$ g)	Total Mass ($\times 10^{16}$ g)	Energy ($\times 10^{31}$ ergs)
		0000 UT 30 May Reconstruction		
12.0	0.30	3.04	4.35	5.6
15.0	0.14	1.84	2.49	3.4
		0000 UT 31 May Reconstruction		
12.0	0.39	2.92	4.16	5.6
15.0	0.19	1.75	2.36	3.3
		0000 UT 30 May North ICME		
15.0	0.030	0.51	0.69	0.9

Table 2. Coronagraph CME Location and Mass

First C2 Appearance							
Date	Time (UT)	Central PA (deg)	Angular Width (deg)	Linear Speed (km/s)	Mass (g) ($\times 10^{14}$) SP	Mass (g) ($\times 10^{14}$) 30° From SP	Mass (g) ($\times 10^{14}$) 60° From SP
27 May 2003	0250:05	90	16	451	0.7	0.9	1.4
27 May 2003	0326:06	60	62	545	23.0	29.0	46.0
27 May 2003	0550:05	293	24	454	2.8	3.5	5.6
27 May 2003	0606:05	91	12	725	0.7	0.9	1.4
27 May 2003	0650:05	Halo (BA)	360	509	–	–	–
27 May 2003	1726:05	2	72	297	6.6	8.3	13.2
27 May 2003	2206:05	215	123	1122	58.0	73.1	116.0
27 May 2003	2350:05	Halo (S)	360	964	–	–	–
28 May 2003	0050:05	Halo (BA)	360	1366	–	–	–
Total mass					91.8	115.7	183.6

[20] Reconstructions for 30 and 31 May are presented in Table 1 to indicate the increase in ICME volume from one day to the next. These two reconstructions show the consistent results for ICME mass and energy on the day the bulk of the ICME has just arrived at Earth, and the next day when the bulk of the material has expanded to a 40% larger size. The last row of Table 1 highlights a more dense mass structure visible to the solar northeast in Figure 10, and determines the excess and total masses within its 0.030 AU^3 volume. This feature can be followed upward in preceding views and is associated with a portion of the LASCO-observed CME that is observed in C2 images starting at 0326 UT on 27 May 2003.

4. Three-Dimensional Reconstruction Comparisons

4.1. LASCO Coronagraph Comparisons

[21] Although several non-halo CMEs observed by the LASCO C2 and C3 coronagraphs in this period have sky plane (SP) masses of less than 10^{16} g, no masses are listed for the full halo CMEs in the LASCO catalog. The omission of SP masses for the full halo CMEs is not surprising since such mass has little meaning for events whose bulk of mass (and thus the CME response) is located far from the coronagraph's SP. Each of the halo CMEs was observed associated with X-ray flares from NOAA active region 10365 located at ~S07 W14 (Solar Geophysical Data, Part II; available at http://sgd.ngdc.noaa.gov/sgd/jsp/solarindex.jsp). As discerned from the LASCO image set available on the Web, the SP brightness of the halo CMEs during this interval are small compared to the brightness of most of the CMEs that are listed in the table and hence the SP masses are undoubtedly also smaller than the other CME masses listed in the catalog, and are assumed here not to contribute significant mass during this period even if traveling at a large angle from the SP.

[22] Table 2 lists a portion of the CME specifications given in the CME catalog on the LASCO Web site (at http://cdaw.gsfc.nasa.gov/CME_list/) for the interval from 0000 UT 27 May 2003, through 0050 UT 28 May 2003; it shows the times, position angle (PA) locations and extents, and SP mass during the interval that have the appropriate onset speeds (assuming the SP speed and the Earth-directed speed the same) and timings to be associated with the observed in situ response at Earth. For the halo CMEs "BA" indicates a halo CME with brightness asymmetry, "S" a halo CME with Symmetry. A coronagraph SP mass is not an exact determination of CME mass but only a lower limit since a CME with excess mass distributed over large distances from

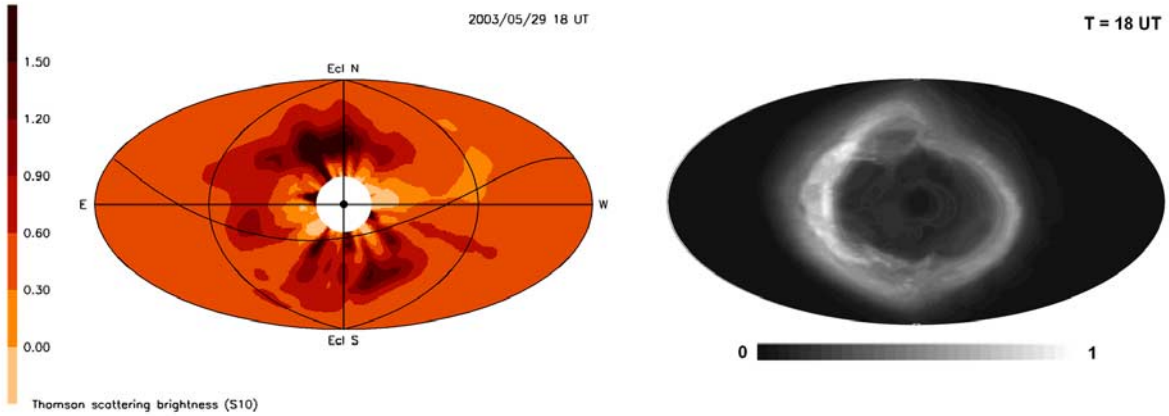

Figure 11. Hammer-Aitoff comparisons of (left) SMEI reconstructed density brightness with the (right) HAF model reconstructed brightness simulation at 1800 UT 29 May 2003. More ICME material is observed in the SMEI analysis to the north and south, and this is associated with CME mass traced outward from the lower coronagraph observations.

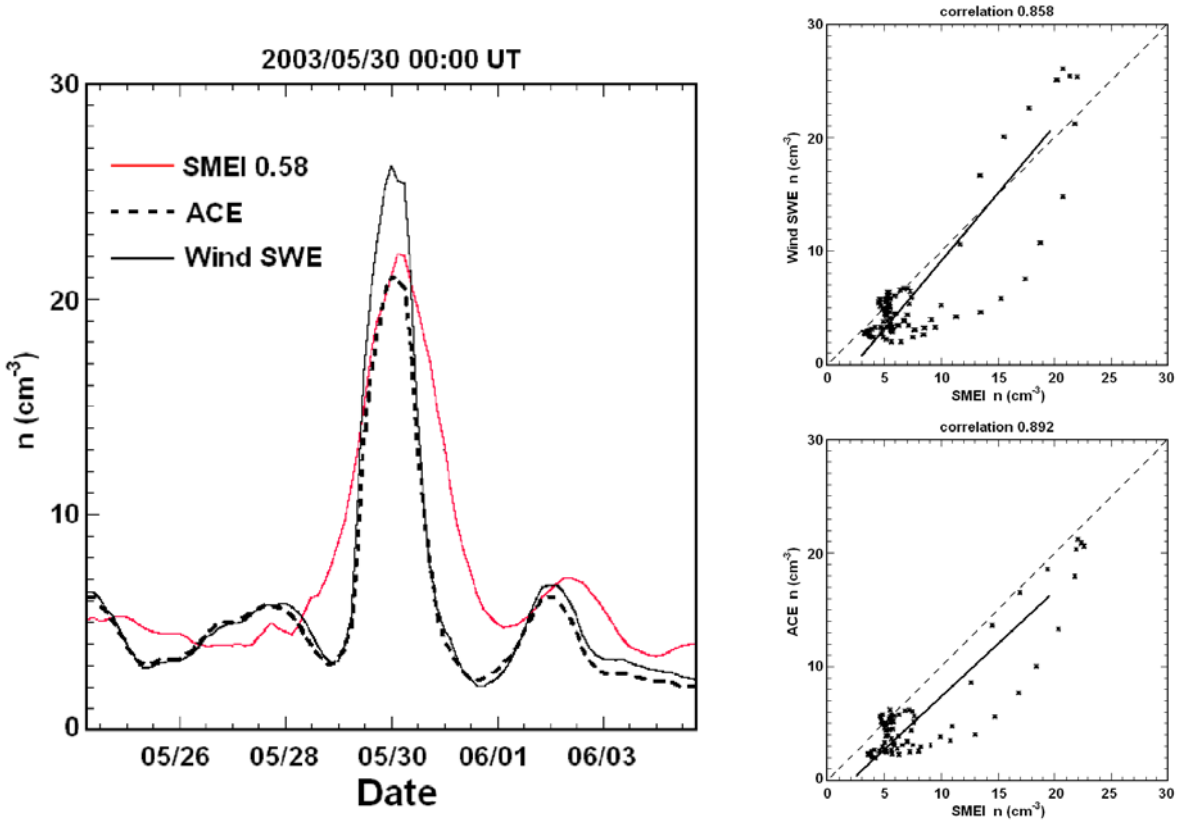

Figure 12. (left) SMEI 3-D reconstructed proton density compared with ACE and Wind in situ data. (right) Correlation over the time interval shown between the 3-D reconstruction and ACE and Wind measurements.

the SP presents less brightness than a CME that is more concentrated there. In addition unless the CME SP location is determined by other means such as these reconstructions coronagraph SP excess masses potentially have large errors because of this unknown factor. The last two columns of Table 2 give the corrected masses for the CMEs, and an estimate of these errors by assuming the CME locations are concentrated at 30° and 60° from the SP, respectively.

[23] The times of the reconstructions shown in Figures 8–10 correspond approximately to the times the bulk of coronagraph CME matter given in this table reaches 1 AU, and so the mass observed in the reconstructions must have been manifest in these earlier eruptions or from solar wind mass. The CME masses from Table 2 can be compared directly with the 1.8 to 3.0 $\times$ 10^{16} g 3-D reconstructed excess ICME mass from Table 1. From the mass totals we see that only if all the coronagraph-observed CME mass in the interval were directed at 60° from the SP (thus within 30° of the Sun-Earth line) would there be enough coronagraph mass to provide the total mass we reconstruct. The largest errors in these comparison determinations come from the inability to define what constitutes the boundaries of the ICME for any given CME. Thus, the total excess coronagraph mass measured in Table 2 in this rough estimate approaches a match with SMEI measurement estimates, but still leaves room for some of the SMEI-observed mass to have been swept up as the CME travels away from the Sun. Finally, from Table 2 we further note that no mass estimate is included for the three halo CMEs, and that the 2206:05 CME contributes 2/3 of the mass but is flagged in the LASCO Web site as a partial halo having an uncertain mass.

[24] Portions of the 3-D reconstructed mass fare better. The CME to the solar northeast first observed in LASCO C3 images at 0326:06 UT is measured as an ICME to total 2.3 $\times$ 10^{15} g. The material in this event can be followed outward in the SMEI reconstructions, and we highlight this mass in Figure 10 (right). Although it is difficult to separate this mass from other ICME-related mass in the vicinity, we measure the solar wind mass excess outlined by the 15 e^{-} cm^{-3} contour at this location to be about 5 $\times$ 10^{15} g of material (see Figure 10). The mass of the associated CME in LASCO coronagraph observations, if 60° from the SP, would be 4.6 $\times$ 10^{15} g and is thus an excellent match. From this exercise, we conclude that a major portion of the reconstructed ICME mass observed near the Earth is associated with the CME expelled mass. The amount of ambient solar wind swept up in the halo CME response can be no more than approximately an equal proportion of mass for this group of events.

4.2. HAF Model Comparisons

[25] Figure 11 presents a comparison of the ICME brightness observed from the SMEI reconstructed density volumes compared with HAF model brightness for this ICME given by *Sun et al.* [2008]. Although the two views show

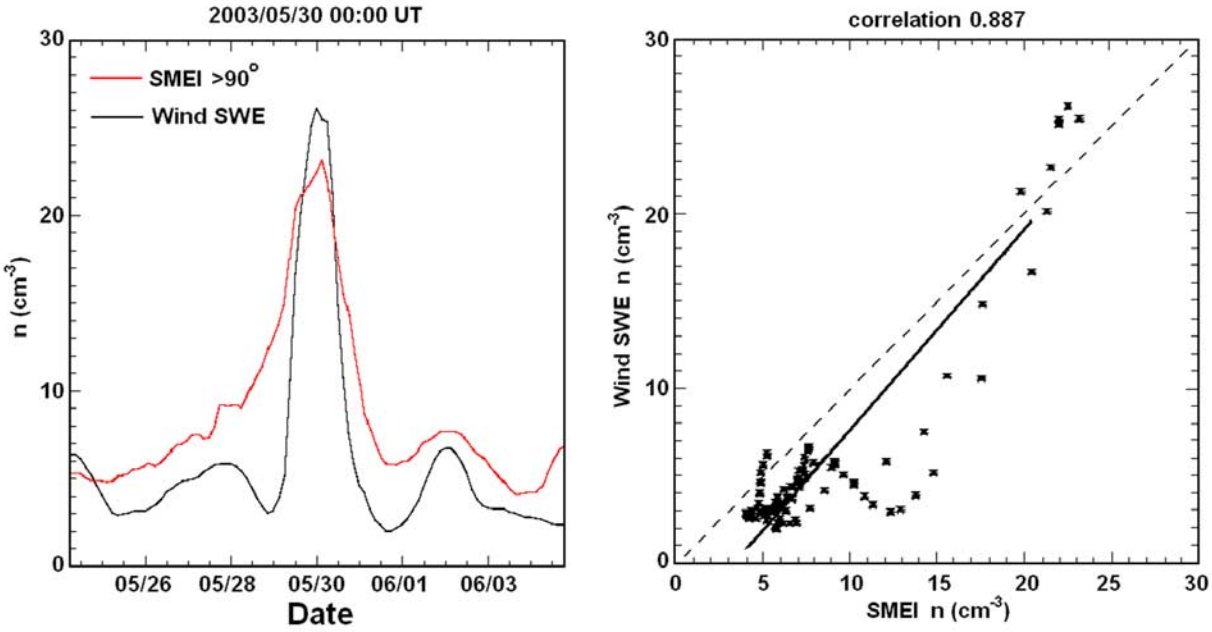

Figure 13. (left) SMEI 3-D reconstructed in situ proton density using only SMEI lines of sight at elongations greater than 90°, here compared with the Wind proton-number-density time series. (right) Correlation over the time interval shown between the 3-D reconstruction and the in situ measurement.

somewhat different brightness variations, the location of the main ICME response looks very similar in each. To match HAF model analyses only the 3-D reconstructed heliosphere on the earthward side of the Sun was used, and as in the fisheye plots of Figures 7c and 7d the SMEI r^{-2} density falloff was included in the presentation of the SMEI brightness as in the HAF display of Figure 11. One notable similarity in the comparison is the somewhat brighter ICME structure to the solar east. *Sun et al.* [2008] attribute this eastward enhancement to deflection of the ICME response and dense material in a corotating interaction region (CIR) that was rotating toward Earth from the east in their simulation. The 3-D reconstructions in Figure 11 as well as Figures 7–10 show this same enhancement in mass to the east of the Sun-Earth line. We note several dissimilarities; the 3-D reconstruction appears broken to the west, and also to the solar southeast. Because of the abundance of SMEI data to the west we expect the reconstruction at this location in the sky to be fairly accurate. The smaller break to the southeast is present where SMEI camera 3 data is absent, and thus the reconstructions here may be more uncertain.

4.3. In Situ Density Comparison

[26] Figure 12 presents the in situ density comparison at 1 AU with measurements of proton densities from the Advanced Composition Explorer (ACE) and Wind spacecraft. To better match the low resolution available in the 3-D reconstructions, ACE hourly averages (as shown in Figure 4) and those from Wind have been smoothed using a 24-h "boxcar" average of adjacent points. There is clearly an extremely good correlation between the 3-D reconstructed density and the in situ density near the main peak. The reconstruction even reproduces a small peak on 2 June. We note that unlike some comparisons between ACE and densities measured by other spacecraft (namely for the Bastille Day 2000 and 28 October 2003 ICME) there is not a large difference found for this event period in the proton density excursions measured by the 5 near-Earth spacecraft (ACE, Genesis, Geotail, SOHO, and Wind). ACE densities over the whole period of the peak enhancement are lower (by 20% over the peak in the Level 2 data and over 40% for the quick look real-time data) than those from the other spacecraft (Wind data are shown in Figure 12). Although brightness in the 3-D reconstructions is matched by the electron density and the Thomson-scattering efficiency factors, as previously noted to obtain the comparisons shown in the 3-D reconstruction and with in situ spacecraft measurements of proton density, a 20% larger number of electrons than protons are used in these reconstructed models commensurate with the ~10% solar wind helium ion abundance by number present in the solar wind at this time.

[27] A somewhat improved comparison between 3-D reconstructed and in situ measurements results for this event when the SMEI lines of sight are restricted to the anti-solar hemisphere of sky observed by SMEI. Figure 13 shows this comparison which is similar to that in Figure 12, but uses only line of sight data from SMEI > 90° elongation. By reconstructing the 3-D volume near Earth from only lines of sight > 90° elongation, the 3-D reconstruction needs only match the material that passes near Earth to provide a comparison with in situ measurements. Solar wind material that emanates from the Sun near its limbs as seen from Earth is not counted in such line-of-sight reconstructions. When this is done the number of valid lines of sight is reduced from 110,000 to 36,000 over the same time interval from 11 May 2003 to 7 June 2003. Moreover, these lines of sight have smaller signal from the portion of the ICME that engulfs the Earth at large elongations (see Figure 4). The reconstruction shows that these 3-D reconstructed density peaks are some-

what smoothed out compared with Figure 12, but they occur at more nearly the correct location in time.

5. Summary and Conclusions

[28] This article shows the white-light Thomson-scattering response of the 27–28 May 2003 CME sequence observed later as an ICME in SMEI observations and their reconstructions in three dimensions. SMEI brightness observations are now calibrated relative to S10 surface brightness to about 4% [*Buffington et al.*, 2007]. This allows a well-calibrated interpretation of the SMEI-brightness observations in terms of line-of-sight electron number using Thomson-scattering coefficients. We present SMEI data in two forms, brightness and 3-D reconstructed proton density. Brightness is originally recorded in ADUs (Figures 3, and 4a and 4b) and is converted to S10 and reconstructed as scattering from electrons (Figures 4c, 4d, and 11). Density is presented as proton number assuming 20% more electrons are associated with each proton owing to the contribution of ionized Helium in order to match with in situ measurements made by spacecraft.

[29] In LASCO observations this particular sequence of halo CMEs shows each moving outward faster than the previous one. Thus each catches up with the preceding such that none are well separated at the present resolution of the SMEI reconstructions when the CMEs arrive near Earth. The ICME mass distribution shows considerable structure within a small fractional AU distance from Earth. This structure is presumably a combination of the more than one CME in the sequence. In addition to mass expelled from the corona associated with the CME sequence, a portion of the inferred ICME mass at Earth is probably also background solar wind material that has been swept up by the faster CME response. Several LASCO CMEs can be followed individually by the SMEI data and 3-D reconstructions into the interplanetary medium. While this specific ICME material is inseparable from other nearby solar wind material, the total ICME mass for specific bright ICME structures is approximately the same as that observed in preceding coronagraph observations. A SMEI 3-D reconstructed total mass for all the ICME components during this interval is about 4×10^{16} g, roughly double the mass inferred from the coronagraph observations. However, to about 20%, this ICME mass determination in the coronagraph CME measurements and in the 3-D reconstructions is critically dependent on the definition used to limit the CME/ICME boundary. This is one of the largest sources of error for this mass measurement. This is the reason we chose in Table 1 to include two different levels for this boundary. As a comparison, the total solar wind ambient mass from $\sim$20 Rs to 1 AU over the entire earthward hemisphere (assuming a constant-velocity solar wind and an ambient of 5 e^{-} cm^{-3} at 1 AU) is also $\sim 4 \times 10^{16}$ g. Considerably more mass than this is available in the ambient solar wind close to the solar surface, where the solar wind has less outward speed. Thus, there is sufficient available solar wind mass in the ambient solar wind, if needed, to provide an additional $\sim 2 \times 10^{16}$ g to the ICME when it is observed near Earth given that a portion of the ICME mass is swept up from the ambient by faster-moving material. On the other hand, within the above factor of two, there is sufficient uncertainty in the mass interpretation from coronagraph observations, including assumptions about the SP location of the observed coronagraph mass, that swept-up material may not be required to provide agreement with the present 3-D reconstructed masses from the SMEI data.

[30] This particular ICME structure is reconstructed as dense material directed toward Earth, and having a larger extent to the north and south of the Earth than to the east and west. The HAF model analysis shows a general structure similar to SMEI reconstructions. Most notably the HAF analysis shows a ring of material that halos the Sun, and this same feature is seen in the SMEI 3-D reconstructed brightness. In addition, the HAF analysis shows a slight enhancement to the solar east, and this same asymmetry is present in SMEI data even though the solar surface location of the energy response required to propagate the HAF-modeled material outward into the heliosphere associated with the halo events is located at $\sim$14° west longitude.

[31] The proton density at Earth from the 3-D reconstruction for this halo CME event sequence gives an ICME peak that correlates extremely well in time and height with in situ proton-density measurements. The peak timing is even better and the cross correlation slightly higher using SMEI data obtained from the anti-solar hemisphere. We expect these correlations can be improved even further, with more lines of sight and thus finer angular resolution, as we further refine the SMEI analysis algorithms and employ more sophisticated 3-D modeling techniques.

[32] **Acknowledgments.** We thank M. Kojima, M. Tokumaru, and the staff at STELab, Nagoya University, Japan, for making available IPS velocity data to us for these analyses under the auspices of a joint CASS/UCSD – STELab cooperative agreement. SMEI was designed and constructed by a team of scientists and engineers from the U.S. Air Force Research Laboratory, the University of California at San Diego, Boston College, Boston University, and the University of Birmingham, UK. We gratefully acknowledge the SOHO/LASCO consortium for making the LASCO images available on the Web and for the listing of the CME masses during the May 27–28 CME interval for use by the Coordinated Data Analysis Workshops (CDAW). The authors also wish to thank the ACE/SWEPAM and Wind/SWE groups for use of their data. The work of B. V. Jackson, A. Buffington, P. P. Hick, and UCSD student J. M. Clover was supported at the University of California at San Diego by NSF grant ATM-0331513 and NASA grants NAG5-134543 and NNG05GG45G. Postdoctoral fellow M. M. Bisi was supported in part by AFOSR grant FA9550-06-1-0107.

[33] Amitava Bhattacharjee thanks the reviewers for their assistance in evaluating this paper.

References

Billings, D. E. (1966), *A Guide to the Solar Corona*, p. 150, Academic, New York.

Brueckner, G. E., et al. (1995), The Large Angle Spectroscopic Coronagraph (LASCO): Visible light coronal imaging and spectroscopy, *Sol. Phys.*, *162*, 357, doi:10.1007/BF00733434.

Buffington, A., D. L. Band, B. V. Jackson, P. P. Hick, and A. C. Smith (2006), A search for early optical emission at gamma-ray burst locations by the Solar Mass Ejection Imager (SMEI), *Astrophys. J.*, *637*, 880, doi:10.1086/498407.

Buffington, A., B. V. Jackson, P. Hick, and S. D. Price (2006), An empirical description of zodiacal light as measured by SMEI, *Eos Trans. AGU*, *87*(52), Fall Meet. Suppl., Abstract SH32A-06.

Buffington, A., J. S. Morrill, P. P. Hick, R. A. Howard, B. V. Jackson, and D. F. Webb (2007), Analyses of the comparative responses of SMEI and LASCO, *Proc. SPIE Int. Soc. Opt. Eng.*, *6689*, 66890B, doi:10.1117/12.734658.

Cox, A. N. (2000), *Allen's Astrophysical Quantities*, 4th ed., Springer, New York.

Eyles, C. J., G. M. Simnett, M. P. Cooke, B. V. Jackson, A. Buffington, P. P. Hick, N. R. Waltham, J. M. King, P. A. Anderson, and P. E. Holladay (2003), The Solar Mass Ejection Imager (SMEI), *Sol. Phys.*, *217*, 319, doi:10.1023/B:SOLA.0000006903.75671.49.

Hick, P. P., and B. V. Jackson (2004), Heliospheric tomography: An algorithm for the reconstruction of the 3D solar wind from remote sensing observations, *Proc. SPIE Int. Soc. Opt. Eng.*, *5171*, 287–297, doi:10.1117/12.513122.

Hick, P. P., A. Buffington, and B. V. Jackson (2005), The SMEI real-time data pipeline: From raw CCD frames to photometrically accurate full-sky maps, *Proc. SPIE Int. Soc. Opt. Eng.*, *5901*, 59011B, doi:10.1117/12.617996.

Hick, P. P., A. Buffington, and B. V. Jackson (2007), A procedure for fitting point sources in SMEI white-light full-sky maps, *Proc. SPIE*, *6689*, 66890B, doi:10.1117/12.734808.

Hildner, E., J. T. Gosling, R. M. MacQueen, R. H. Munro, A. I. Poland, and C. L. Ross (1975), The large coronal transient of 10 June 1973 I: Observational description, *Sol. Phys.*, *42*, 163, doi:10.1007/BF00153293.

Jackson, B. V., and P. P. Hick (2002), Corotational tomography of heliospheric features using global Thomson scattering data, *Sol. Phys.*, *211*, 345, doi:10.1023/A:1022409530466.

Jackson, B. V., and P. P. Hick (2004), Three-dimensional tomography of interplanetary disturbances, in *Solar and Space Weather Radiophysics: Current Status and Future Developments*, *Astrophys. Space Sci. Libr.*, vol. 314, edited by D. G. Gary and C. U. Keller, p. 355, Kluwer, Dordrecht, Netherlands.

Jackson, B. V., P. L. Hick, M. Kojima, and A. Yokobe (1998), Heliospheric tomography using interplanetary scintillation observations, 1. Combined Nagoya and Cambridge observations, *J. Geophys. Res.*, *103*, 12,049, doi:10.1029/97JA02528.

Jackson, B. V., A. Buffington, and P. P. Hick (2001), A heliospheric imager for solar orbiter, in *Proceedings of Solar Encounter: The First Solar Orbiter Workshop, Puerto de la Cruz, Tenerife, Spain, 14–18 May 2001*, *Eur. Space Agency Spec. Publ.*, *ESA SP-493*, 251.

Jackson, B. V., P. P. Hick, and A. Buffington (2002), Time-dependent tomography of heliospheric features using the three-dimensional reconstruction techniques developed for the Solar Mass Ejection Imager (SMEI), *Proc. SPIE Int. Soc. Opt. Eng.*, *4853*, 23.

Jackson, B. V., et al. (2004), The Solar Mass Ejection Imager (SMEI) mission, *Sol. Phys.*, *225*, 177, doi:10.1007/s11207-004-2766-3.

Jackson, B. V., A. Buffington, P. P. Hick, X. Wang, and D. Webb (2006), Preliminary three-dimensional analysis of the heliospheric response to the 28 October 2003 CME using SMEI white-light observations, *J. Geophys. Res.*, *111*, A04S91, doi:10.1029/2004JA010942.

Jackson, B. V., P. P. Hick, A. Buffington, M. M. Bisi, M. Kojima, and M. Tokumaru (2007a), Comparison of the extent and mass of CME events in the interplanetary medium using IPS and SMEI Thomson scattering observations, *Astron. Astrophys. Trans.*, *26*(6), 477–487, doi:10.1080/10556790701612221.

Jackson, B. V., P. P. Hick, A. Buffington, M. M. Bisi, and E. A. Jensen (2007b), SMEI observations in the STEREO era, *Proc. SPIE Int. Soc. Opt. Eng.*, *6689*, 66890G, 1–14, doi:10.1117/12.734870.

Kojima, M., M. Tokumaru, H. Watanabe, A. Yokobe, K. Asai, B. V. Jackson, and P. L. Hick (1998), Heliospheric tomography using interplanetary scintillation observations: 2. Latitude and heliocentric distance dependence of solar wind structure at 0.1–1 AU, *J. Geophys. Res.*, *103*, 1981, doi:10.1029/97JA02162.

Mizuno, D. R., et al. (2005), Very high altitude aurora observations with the Solar Mass Ejection Imager, *J. Geophys. Res.*, *110*, A07230, doi:10.1029/2004JA010689.

Sun, W., C. S. Deehr, M. Dryer, C. D. Fry, Z. K. Smith, and S.-I. Akasofu (2008), Simulated Solar Mass Ejection Imager and "Solar Terrestrial Relations Observatory-like" views of the solar wind following the solar flares of 27–29 May 2003, *Space Weather*, *6*, S03006, doi:10.1029/2006SW000298.

Tappin, S. J., et al. (2004), Tracking a major interplanetary disturbance with SMEI, *Geophys. Res. Lett.*, *31*, L02802, doi:10.1029/2003GL018766.

Webb, D. F., et al. (2006), Solar Mass Ejection Imager (SMEI) observations of coronal mass ejections (CMEs) in the heliosphere, *J. Geophys. Res.*, *111*, A12101, doi:10.1029/2006JA011655.

Yu, Y., P. P. Hick, and B. V. Jackson (2005), Interactive visualization of Solar Mass Ejection Imager (SMEI) volumetric data, *Proc. SPIE Int. Soc. Opt. Eng., 5901*, *59011a*, 1–5.

M. M. Bisi, A. Buffington, J. M. Clover, P. P. Hick, and B. V. Jackson, Center for Astrophysics and Space Sciences, University of California, San Diego, 9500 Gilman Drive, #0424, La Jolla, CA 92093-0424, USA. (bvjackson@ucsd.edu)

W. Sun, Geophysical Institute, University of Alaska, Fairbanks, AK 99775-7320, USA.